

Article

Development of a Polymeric Arrayed Waveguide Grating Interrogator for Fast and Precise Lithium-Ion Battery Status Monitoring

Jan Meyer ^{1,*}, **Antonio Nedjalkov** ^{1,2}, **Elke Pichler** ², **Christian Kelb** ¹ and **Wolfgang Schade** ^{1,2}

¹ Department for Fiber Optical Sensor Systems, Fraunhofer Heinrich Hertz Institute, 38640 Goslar, Germany; antonio.nedjalkov@hhi.fraunhofer.de (A.N.); christian.kelb@hhi.fraunhofer.de (C.K.); wolfgang.schade@hhi.fraunhofer.de (W.S.)

² Institute of Energy Research and Physical Technologies, Clausthal University of Technology, 38640 Goslar, Germany; elke.pichler@tu-clausthal.de

* Correspondence: jan.meyer@hhi.fraunhofer.de

Received: 10 September 2019; Accepted: 14 October 2019; Published: 18 October 2019



Abstract: We present the manufacturing and utilization of an all-polymer arrayed waveguide grating (AWG) interacting with a fiber Bragg grating (FBG) for battery status monitoring on the example of a 40 Ah lithium-ion battery. The AWG is the main component of a novel low-cost approach for an optical interrogation unit to track the FBG peak wavelength by means of intensity changes monitored by a CMOS linear image sensor, read out by a Teensy 3.2 microcontroller. The AWG was manufactured using laser direct lithography as an all-polymer-system, whereas the FBG was produced by point-by-point femtosecond laser writing. Using this system, we continuously monitored the strain variation of a battery cell during low rate charge and discharge cycles over one month under constant climate conditions and compared the results to parallel readings of an optical spectrum analyzer with special attention to the influence of the relative air humidity. We found our low-cost interrogation unit is capable of precisely and reliably capturing the typical strain variation of a high energy pouch cell during cycling with a resolution of 1 pm and shows a humidity sensitivity of $-12.8 \text{ pm per } \%RH$.

Keywords: arrayed waveguide grating (AWG); CMOS sensor; direct laser lithography; fiber Bragg grating (FBG); lithium-ion battery

1. Introduction

Lithium-ion batteries have become the foundation of a wide variety of applications depending on electrochemical energy storage [1], starting with small single cells in billions of mobile phones [2] to a vigorously growing amount of electric vehicles [3] and large battery storage power stations [4], although the latter is oftentimes viewed critically under economic aspects [5]. Regardless of the size or scope, all lithium-ion batteries have in common the need to be meticulously monitored in order to ensure safe and durable operation. This type of electrochemical energy storage only has a small range of tolerated operational states [6] and tend toward exothermic reactions, usually referred to as thermal runaway (TR) [7], if the limits for safe operation are violated.

If voltage or temperature specifications are violated, the resulting fire can quickly propagate through densely packed battery systems, causing the TR of neighbored cells and ultimately of the whole system. A number of accidents have already attracted public attention in the past [8] and it is safe to say, that, with increasing number of electric cars and high-powered stationary applications this attention will increase.

Additional to ensuring operational safety, adequate status monitoring enables the user to decide whether a lithium-ion battery may be used any further [9]; for example, a used traction battery with an insufficient capacity may still operate fine in low power stationary applications. Extended monitoring of lithium-ion batteries therefore can affect the economic treatment of used batteries [10] as e.g., either waste or valued energy storage systems for stationary applications.

State-of-the-art monitoring systems for lithium-ion batteries consist almost exclusively of electronic battery management systems (BMS) that obtain their information from electrical sensors [11]. The most frequently obtained measurement quantities are voltage, temperature and current. While voltage is usually acquired for each cell, current and temperature are often measured for modules and/or whole battery packs. A wide variety of methods for determining the state of charge (SOC) is currently utilized ranging from simple charge counting over model-based observers to neural networks and fuzzy logic algorithms. All methods yield a SOC accuracy equal or below 6% although diminishing capacity due to wear on the battery is not modeled in SOC estimation. State of health (SOH) estimation is therefore carried out in parallel fashion [12,13], using e.g., different battery models and the results are fed into the mostly adaptive SOC algorithms.

However, most applied methods still lack on accuracy and a safety margin for allowed battery SOC and SOH is usually applied to account for uncertainties and avoid financial damages e.g., due to warranty claims.

Additional information about the SOH of a lithium-ion battery would therefore be desirable and can for instance be obtained by strain sensors due to increasing distension over the lifetime, causing e.g., strain on clamped battery packs [14]. Electric strain sensors however are only partially suited for the task, since precise measurement is only possible using bulky 3- or 4-wire connections and strong electric currents inside the battery system can impact the measurement.

One well-known optical method for strain and temperature measurement is the application of fiber Bragg gratings (FBG), which combine many advantages [15]. They are small and lightweight, and a large number of sensor elements can be cost-effectively integrated in a single glass fiber, thus reducing cabling complexity. They are mostly insensitive to electric and magnetic fields and able to withstand high temperatures of several hundred degrees Celsius [16,17].

FBG sensors have already been used for status monitoring of lithium-ion batteries by different research groups [18], since they are capable of delivering information beyond conventional BMS. They can serve as simple temperature sensors [19,20], outside and even inside of a cell [21,22], or as functionalized sensor elements that are sensitive to chemical substances and their optical properties [23,24]. Additionally, due to the small fiber diameter of 125 μm , FBG sensors can be integrated in many areas that are usually inaccessible for electric sensors e.g., in a battery system consisting of many densely stacked cells. FBG, applied as external strain sensors for monitoring lithium-ion cells with a flexible casing (also referred to as pouch cells), have been demonstrated several times already [25–27]. This observable strain variation during operation is of great interest for an improved state estimation because none of the aforementioned methods used in practice are capable of delivering information about the mechanical behavior of the cells, e.g., swelling due to aging effects.

For the readout of FBG sensors, several different interrogators exist [28]. Interferometric methods [29,30], tunable-filter-based interrogation methods [31] or methods with conversion from the wavelength domain to the time domain [32] are described in literature. All mentioned methods however are realized in discrete, bulky optical setups, built and adjusted by hand, even in the case of commercial devices and not robust enough, e.g., against vibrations, for reliable utilization in automotive applications.

Arrayed waveguide gratings (AWG), commonly used as (de)-multiplexing devices in telecommunications [33], are also well known as FBG interrogators for many years and their advantages, such as high number of output channels, wide bandwidth, precise wavelength detection, high-speed capability and low cost, have been reported [34]. Additionally, their compact, integrated design leads to a certain robustness that discrete systems cannot offer.

Most AWG are made of silicon and operate at wavelengths around 1550 nm [35]. In special applications—as it is the case with FBG-based battery monitoring at least today—the costs of manufacturing process setup as well as the cost-per-unit for silicon AWG is so high, that we could find no scientific or commercial implementation of AWG-based readout for fiber optic battery sensors despite the huge advantages. We therefore manufactured all-polymer AWG that are working at near IR center wavelength (850 nm), reducing manufacturing complexity, post-processing effort and resulting per-unit cost dramatically, as described in [36]. A further advantage of the unit working in the 850 nm region lies in lower cost of peripheral components like light sources and detectors.

Here, we present to our knowledge the first interrogation system based on an all-polymer AWG that is read-out by a CMOS linear image sensor and utilized as a readout-device for fiber optic battery sensors.

2. Sensor and System Design

In the following subsections, the key components of the novel interrogation system are presented consecutively. Although the mathematical modeling, simulation and general fabrication steps for an all-polymeric AWG have been recently presented [36] and are not part of this work, the design and manufacturing are described as differences exist.

2.1. Arrayed Waveguide Grating Fabrication

The AWG is the central sensor component of the experiments carried out in this work. The main goal, therefore, is to realize a reproducible and long-term stable status monitoring with an all-polymer AWG, which also achieves the required measurement accuracy for this purpose. Since initially only one optical measuring point is to be evaluated, in the first development step, an AWG with one input and three output channels is utilized. The latter have their intensity maximum at the wavelengths 850.6, 851.6 and 852.6 nm, respectively.

Before production, an optical simulation is performed with a commercially available software program (Epiprop, Photon Design), taking into account the refractive index data and attenuation losses of the materials used as well as the resolution capability of the production machine applied. In order to minimize possible stray light effects, input and output waveguides should have an angular offset of 90°. The simulation result represents a compromise of high transmission efficiency, high channel sensitivity and low modal dispersion. The finalized design consists of 50 single arrayed waveguides with a grating order of 40 and a radius of 1.5 mm. At the input and output of this arrayed waveguides, the two free propagation zones are arranged, which each are assigned a length of 4.0 mm by the simulation. For the best possible light wave guidance at the relevant wavelength, a layer height of the entire polymeric structure of 3.2 μm is determined. The AWG is calculated with a waveguide width of 5.2 μm causing all waveguides to guide a second mode over the fundamental one. Due to the manufacturing process, a minimum distance of 1.0 μm must be maintained between the individual waveguides, which correlates with the minimum pattern size of the applied sensor structuring direct laser lithography machine ($\mu\text{PG} 101$, Heidelberg Instruments). This resolution also dictates the non-single-mode waveguides—however, the negative effects of this are satisfactorily compensated by the relatively low grating order.

In the next step, a graphic production template for the fabrication is created from the simulation result. As substrate material Cyclo-olefin polymer (COP, Zeonex® flexible foil, Microfluidic ChipShop, Jena, Germany) with a thickness of 188 μm is used. Its surface is treated with oxygen plasma for 1 min (Plasma Prep, Gala Instruments, Bad Schwalbach, Germany) to effect favorable adhesion with the photoconductive polymer, which consists of an inorganic–organic copolymer system (EpoCore/EpoClad, microresist technology). At first, EpoClad as the lower cladding with a refractive index of 1.5708 is spin-coated to a height of 2 μm . This layer is then pre-baked for 5 min at 120 °C, subsequently cured by 365 nm UV flood exposure and lastly hard-baked for 60 min at 120 °C. After another surface plasma treatment for 1 min, EpoCore as the light-guiding patterned material with a refractive index of 1.5836

is spin-coated to a height of 3.2 μm . According to the graphic template, the sensor element structure is created by laser direct patterning with the lithography machine at a wavelength of 375 nm and a power of 6 mW. This is followed by a post-bake phase for 5 min at 90 °C, before the non-cured areas are removed with the developer (mrDev600, microresist technology). The remaining cured AWG structure is subsequently hard-baked for 60 min at 120 °C. In the last step, EpoClad as upper cladding is again applied with a height of 20 μm by spin coating, hereafter pre-baked, UV flood exposed and finally post-baked. In Figure 1, a total-view microscope image of the AWG structure and associated height profile measurements are shown.

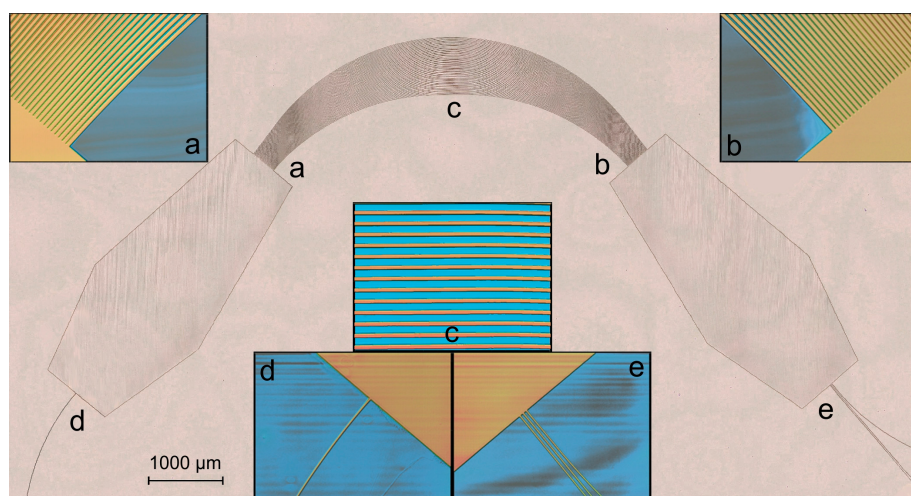


Figure 1. Laser scanning microscope images of the arrayed waveguide grating (AWG) manufactured with the described parameters. Between the end of the first free propagation zone (a) and the beginning of the second free propagation zone (b), the 50 arrayed waveguides are arranged (c). At the entrance to the first free propagation zone is the input waveguide (d) and at the exit of the second free propagation zone are the three output waveguides (e). The height of the entire structure is homogeneously 3.2 μm .

In order to have low insertion losses, the input waveguide is vertically cut and then polished. The output waveguides are treated in the same way. In the next section, the integration of the polymer AWG into the interrogator is described.

2.2. Interrogator Design

The previously presented AWG is the main component of the interrogator. To eliminate influences of the temperature on the optical properties of the AWG, it is fixed to an isothermal plate with a set temperature of 25 °C and regulated by a Peltier controller (MTD415L, Thorlabs). After polishing, a single-mode fiber is glued to the AWG polymeric input waveguide. At the other end of the fiber, a FC/APC connector is attached and is connected to a fiber port. The output waveguides face directly to a vertical CMOS linear image Sensor (iC-LFH1024, iC-Haus, Bodenheim, Germany). The sensor has a total of 1024 pixels, each with 600 μm height and 12.7 μm width. The output with its intensity maximum for a wavelength of 852.6 nm is positioned at pixel 407, the output with its intensity peak at a wavelength of 851.6 nm is positioned at pixel 486, and the third output with its intensity maximum at a wavelength of 850.6 nm is positioned at pixel 565, respectively. The descending order of wavelength at an increasing order of pixel number is simply because the CMOS linear image sensor is fixed up-side-down to the isothermal plate for easier connectorization. The CMOS linear image sensor is controlled and read-out by a microcontroller (Teensy 3.2, PJRC), that transmits its data via USB to a primary computer where they are processed further. The described components are placed in a lightproof aluminum casing. A schematic overview is shown in Figure 2.

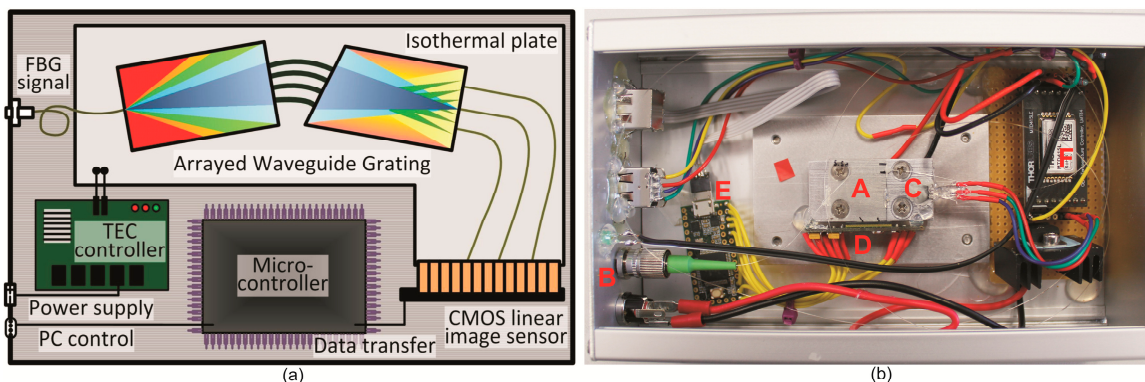


Figure 2. Schematic (a) and photographic (b) overview of the AWG interrogator. The polymeric AWG (A) is connected with a single-mode fiber (B) at the input and fixed on an isothermal plate (C). The output waveguides end facets are attached directly to the vertical CMOS linear image sensor (D). The CMOS sensor is read-out by a microcontroller (E). The TEC controller (F) is also allocated within the system.

2.3. Fiber Bragg Grating Fabrication

For the production of the FBG, a femtosecond pulsed laser-based point-by-point inscription method is applied. With a three-dimensional computer-controlled translation stage (N-565.260 linear translation stage, Physik Instrumente (PI), Karlsruhe, Germany) and an objective lens (LD Plan-Neofluar 20 \times , Zeiss, Oberkochen, Germany), the utilized standard telecommunication single-mode glass fiber (SMF810-E5/125PI, Leoni, Nuremberg, Germany) is optically focused on its light-guiding core. During processing, pulses from a femtosecond laser (Ti:Sapphire Tsunami/Spitfire pro, Spectra-Physics, Santa Clara, CA, USA) pass the lens and form single grating points with a locally increased refractive index. The fiber is moved by the translation stage after each pulse until the entire type II fiber Bragg grating is produced. Due to the adaptability of this manufacturing method, the properties of the gratings can be systematically customized to the requirements of the respective polymer AWG channels. For the current experimental version, a Bragg grating with a central reflection wavelength of 852.30 nm, a peak width at half-height of 0.90 nm and a reflectivity of 90.0% is manufactured (figure of spectrum in the appendix). To suppress interfering secondary modes, linear shape apodization is used. With a grating length of 1.15 mm comprising of 700 single refractive index modifications, a reflection spectrum approximately shaped like an ideal Gaussian curve can thus be generated. This shape is particularly suitable for calibrating the AWG channels as described in the following section.

2.4. System Calibration

In order to obtain the correlation between light intensity at the end of the output waveguides and the central wavelength of the narrowband spectrum reflected by the FBG at the AWG input, a wavelength calibration is done, and the results are shown in Figure 3. The setup for the system calibration is largely similar to the one for the battery experiments that are presented in the following section. It mainly consists of the FBG, the AWG, an optical spectrum analyzer (OSA) (AQ6373B, Yokogawa, Tokyo, Japan) and a superluminescent diode (SLED) (EXS210037-01, Exalos, Schlieren, Switzerland). The major difference is that the FBG is not fixed to the battery cell at this point. Instead, the FBG, described in the previous section, is fixed with one end to a manual translational stage (NanoMax-TS Max302/M, Thorlabs, Newton, MA, USA) and with the other end to a rigid post. At a room temperature of 21 °C, the FBG is randomly stretched by incrementally moving the translational stage, resulting in a shift of the reflected wavelength between 852.5 nm and 853.25 nm. The broadband light spectrum of the SLED is launched into the fiber beginning and partly reflected at the FBG from where it is guided via a 3dB coupler (FC850-40-50-APC, Thorlabs, Newton, MA, USA) to the input of the AWG. The remaining spectrum, reduced by the reflected spectral range, is transmitted to the end

of the fiber, where the actual FBG wavelength is evaluated by the OSA. This reference value is stored together with the intensities at the three AWG output waveguides, that as a result of the reflected FBG signal at the input, are captured by the CMOS sensor. To minimize possible errors, due to AWG waveguide outputs positioned between two pixels of the CMOS linear image sensor, the intensities of the pixel before and after the aforementioned pixels (407, 486, 565) are also taken into account and an averaged value is calculated.

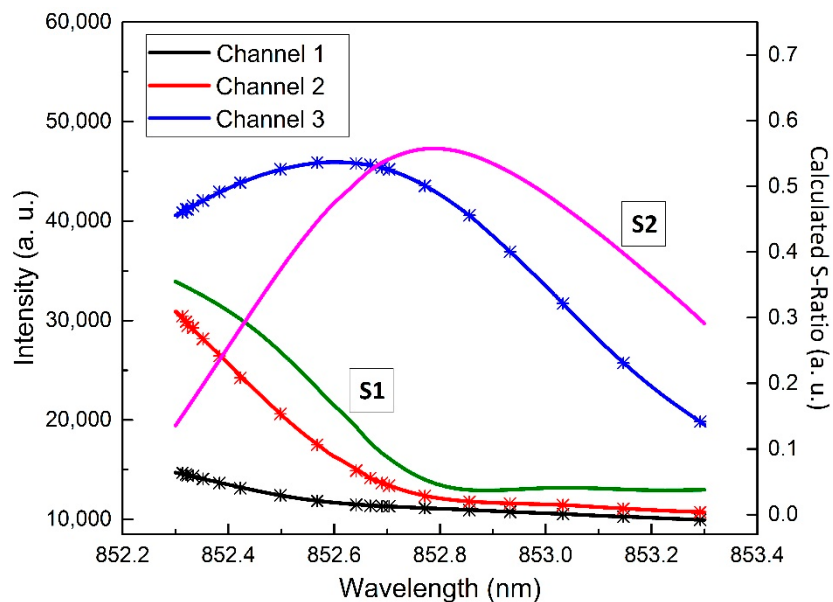


Figure 3. Correlation between center wavelength of the light portion reflected at the fiber Bragg grating (FBG) and the averaged intensities of the CMOS pixels at the AWG output waveguide positions. By using the fitted values as inputs for Equation (1), the green S-ratio course was calculated for channel 1 and 2 and the magenta S-ratio course was calculated for channel 2 and 3, respectively.

Subsequently, the intensities are used to interpolate the course of the AWG output signals with respect to the center wavelength of the light portion reflected by FBG. Finally, according to [37], the ratio between the difference of two adjacent channel intensities over their sum is calculated, as shown in Equation (1), where I_i is the averaged intensity of channel i .

$$S_i = (I_{i+1} - I_i) / (I_{i+1} + I_i) \quad (1)$$

The ratio S is calculated depending on the reflected wavelength and stored with a resolution of 1 pm as a look-up table in the analysis software, in order to obtain an expression for the wavelength that is independent from the power of the light source as well as from the integration time of the CMOS image sensor. The integration time for all experiments presented here is set to 10 ms and usually 50 scans were averaged, thus an overall data acquisition frequency of 2 Hz results.

3. Results and Discussion

To demonstrate the performance of the new polymeric AWG interrogator, long-term experiments with the presented FBG sensor were conducted. The optical sensor, in this particular case, serves predominately as a strain sensor since it is fixed to the surface of a lithium-ion pouch cell by means of instant adhesive. Although, FBG sensors are sensitive to both temperature and strain, the reader should note that for the cyclization experiments presented in this paper, the shift in reflected wavelength is almost exclusively due to strain because the current rate is low and the resulting heat generation of the cell minimal. Furthermore, the cell is placed in a temperature regulated environment, first to investigate the shift of the reflected wavelength due to changes of the temperature (part A) and

second to ensure a constant temperature during the cycling experiments (part B). The AWG interrogator is placed along with the light source and the coupler in a separate temperature chamber that is set to a constant temperature of 16 °C. The intensity signals transmitted from the microcontroller are processed by a personal computer in the analysis software in which the previously obtained relationship between intensities and FBG wavelength is calculated, displayed and finally stored. The overall experimental setup is schematically shown in Figure 4.

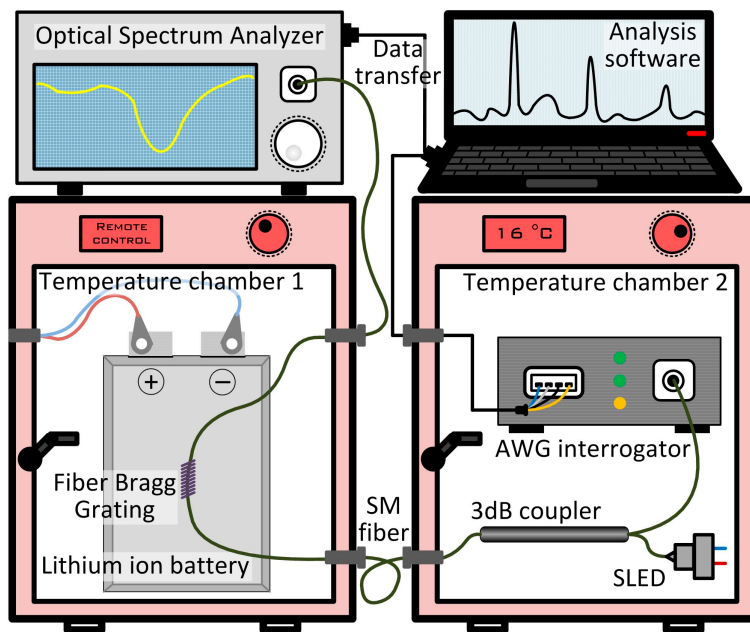


Figure 4. General setup for the temperature (part A) and cyclic experiments (part B). The AWG interrogator, along with the superluminescent diode (SLED) light source, and the fiber-coupler are put into a temperature chamber with a constant temperature of 16 °C and a constant relative humidity of 43% (only for part B). The investigated lithium-ion cell is put in a temperature chamber with a variable temperature for experimental part A and a constant temperature of 20 °C for experimental part B, respectively. The cell is electrically connected to a battery cyclization unit and optically connected to the AWG as well as to the optical spectrum analyzer (OSA). The AWG evaluates the FBG wavelength through the reflected spectrum and the OSA evaluates it through the transmitted spectrum.

3.1. Temperature and Humidity Variation

In order to ascertain a proper fixing of the FBG to the lithium-ion cell surface and to gain information about the influence of the cell temperature as well as of the relative air humidity on the reflected wavelength, first, the cell is exposed to temperature variations. For this purpose, the temperature chamber 1 is set to 20 °C for a sufficiently long time, followed by a step to 25 °C, and after a rest time of 4 h, the temperature is increased by a step of 5 K again. The temperature is held at 30 °C for 4 h and afterwards the temperature is decreased to 20 °C again, by means of 5 K steps, with the same resting periods as during temperature raise. These steps are conducted two times, followed by 40 h with constant temperature. The results can be seen in Figure 5.

During the experiment, relative humidity of the surrounding air in the temperature chamber 2 is additionally recorded with a digital sensor (HYT 939, Innovative Sensor Technology, Ebnat-Kappel, Switzerland). As a result of the regional weather changes, the values for the relative air humidity vary between 45%–55% inside the non-air-conditioned laboratory. For the isothermal period starting from experiment hour 30, no change of the reflected wavelength is expected and almost none is measured by the OSA. Nevertheless, the variation of the reflected wavelength measured by the AWG is 110 pm, as shown in Figure 5.

It is well known that polymeric plastics in general and the EpoClad/EpoCore photoresists used within this research work in particular are hygroscopic [38], and the absorption of water molecules, in turn, changes the optical properties of the AWG. In Figure 6, it can be seen, that for the herein presented humidity range, a linear relationship, including a hysteresis, exists.

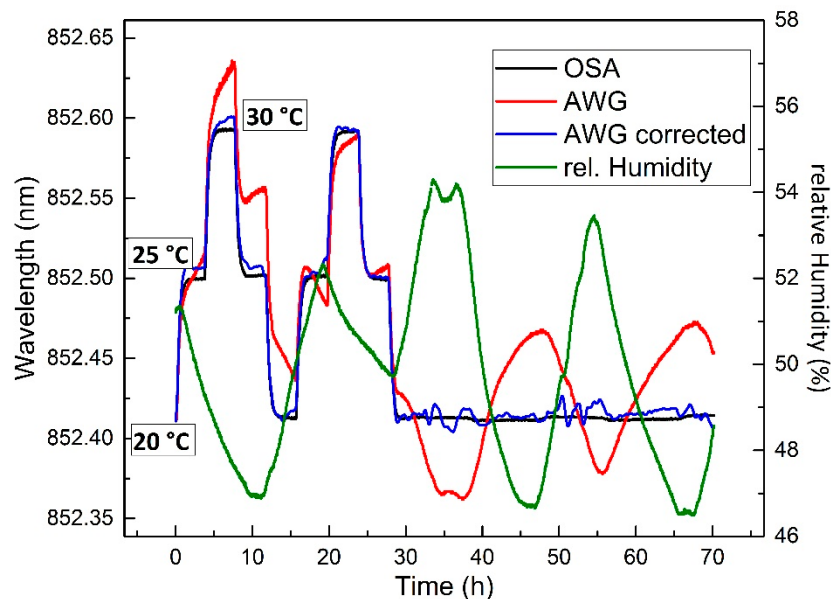


Figure 5. FBG wavelength measured by the OSA and the AWG, respectively, during the temperature experiment together with the relative air humidity in the surrounding of the AWG. The humidity strongly influences the optical properties of the AWG. The corrected AWG values (blue course) are calculated by using Equation (2).

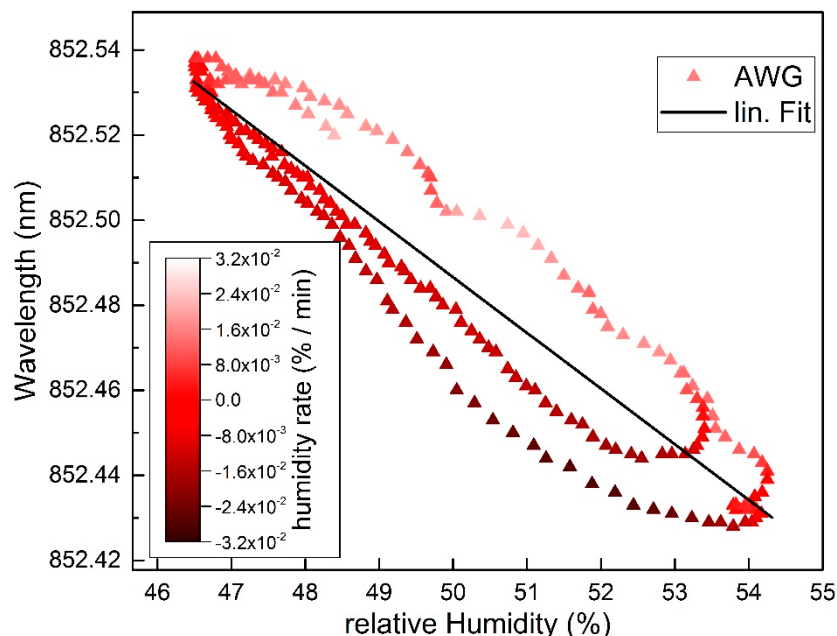


Figure 6. FBG wavelength measured by the AWG during the isothermal period of the temperature experiment shown in Figure 5. In the relevant humidity range there is a linear correlation between the optical output of the AWG and the relative humidity.

To minimize the variation of the AWG output due to the change of relative humidity, a multiple linear regression fit is done, expressed by Equation (2), where ξ is the relative air humidity in percent and $\dot{\xi}$ the change of the relative humidity in %/min. Λ is the regression constant determined to 853.1 nm, α and β are coefficients determined to $-0.0128 \text{ nm}/\%$ and $0.9077 \text{ nm}\cdot\text{min}/\%$, respectively. Λ_c , as the result of Equation (2), represents the corrected wavelength, shown as the blue course in Figure 5.

$$\Lambda_c(\xi, \dot{\xi}) = \Lambda + \alpha \xi + \beta \dot{\xi} \quad (2)$$

The disturbance-related variation of the AWG values can be decreased to 20 pm during the isothermal period by applying Equation (2). The deviation from the values measured by the OSA during change of the temperature is also improved.

3.2. State of Charge Variation

Although the influence of the relative air humidity is known and can be minimized, the relative air humidity in temperature chamber 2 is kept constant ($43.4\% \pm 0.9\%$) by using a vessel with a saturated salt solution of potassium carbonate (K_2CaO_3) for the long-term cyclization experiment. Furthermore, the temperature of the temperature chamber 1 is set to 20°C during the whole time, thus the Bragg sensor is particularly sensitive to changes of the cell's surface strain.

In Figure 7, the result of the cyclic experiment is shown. For a time of 27 days, the lithium-ion cell underwent 25 full charge–discharge cycles with a current of 5 A between 4.2 V and 3.0 V. It can be seen that the reflected wavelength signal, measured by the AWG, is in good agreement to the signal measured by the OSA in the transmitted spectrum.

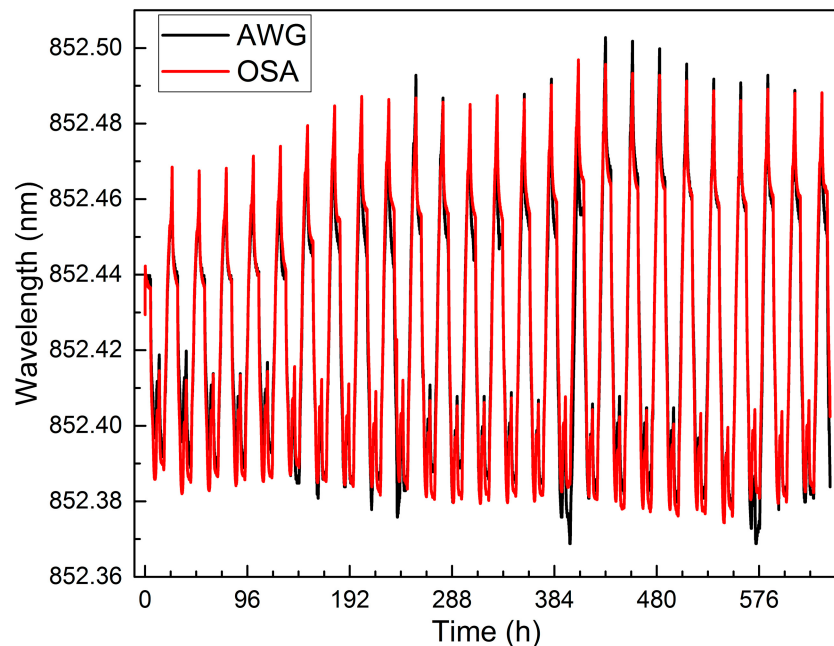


Figure 7. Result of the cyclization experiment. Over 27 days, 25 cycles are performed. The AWG signal is in good agreement to the OSA signal at any time and represents the battery status well.

For every time step, the error of the AWG is shown in Figure 8, along with the values for the relative humidity. Even though the maximum error is in the range of 3×10^{-2} nm during the 16th cycle (at experiment time 390), the total mean error is 6.5×10^{-4} nm, with a standard deviation of 5.9×10^{-3} nm. Furthermore, it is evident that the largest deviation between OSA and AWG occur when there are significant variations of the relative humidity, like in hour 240, 408 and 576, respectively.

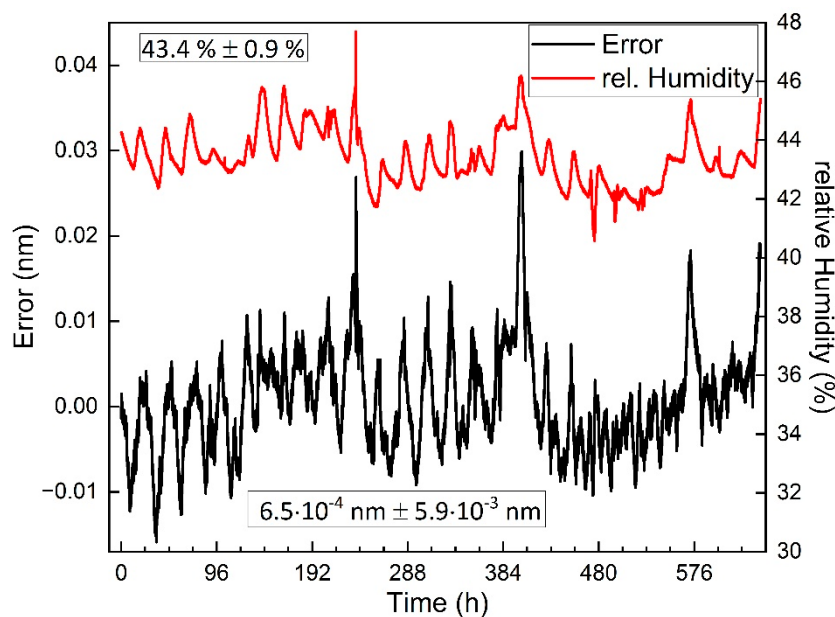


Figure 8. Difference between AWG and OSA signal together with the relative humidity. The largest errors occur when there are great variations in the humidity.

From this long-term experiment, an estimation of both the accuracy and precision of our system can be derived. At the selected settings, our Yokogawa AQ6373B optical spectrum analyzer features a wavelength accuracy of $\pm 5 \times 10^{-2}$ nm and a resolution of 2×10^{-2} nm. The above-described error between OSA and AWG adds to that, so that the accuracy of our system can be calculated to $\pm 7.59 \times 10^{-2}$ nm.

To demonstrate the eligibility of the presented polymeric AWG interrogator as a useful device for the status monitoring of lithium-ion cells, one single cell charge–discharge cycle is shown in detail in Figure 9. The cell charging starts at experiment hour 601 when the cell voltage rises significantly and the first drop in the wavelength takes place. This is caused by a typical temperature decrease at the beginning of the charge process, since endothermic chemical processes are predominant over the Joule heat generation. In the ongoing course, the reflected wavelength begins to rise, as the lithium-ions intercalate to the anode, causing an increase of the cell’s volume and therefore of the surface strain. Reference [39] demonstrates the correlation between the graphite anode potential (vs. Li/Li⁺) of a lithium-ion battery and its intercalation stages. This can be seen in Figure 9 by different voltage rates of change that are typical for lithium-ion cells. The optical signal also has a nonlinear course and shows different rates of change, which makes them suitable for the detection of characteristic phase transition points that can be used for status monitoring of lithium-ion batteries, although the exact correlation between voltage signal and volumetric behavior is not fully understood yet.

The charging terminates at the signal peak at experiment hour 609.5, followed by a rest period of 5 h, during which a relaxation of the cell takes place. The voltage signal decreases only slightly but a larger decrease in the strain signal occurs, showing ion diffusion processes on the one side and a temperature approximation to the ambient temperature on the other side. It is known that this behavior can also change with an ongoing degradation of the cell because the open-circuit voltage of a lithium-ion cell is linked to its capacity, what can be used to determine the actual SOC or SOH, for example by performing incremental capacity analysis [40].

The discharge cycle starts at hour 615 and is identifiable by a sudden decrease of the voltage signal and the reflected wavelength. Similar to the charging period, the course of the voltage signal shows again characteristic rate changes at certain points caused by the deintercalation of the lithium-ions from the graphite anode and it can be seen in Figure 9 that the strain course also changes at these points. At the end of the discharge cycle at experiment hour 619, the signal rises again, which is due

to a significant temperature rise, caused by a typically increasing internal cell resistance that leads to increased Joule heating. After discharge, the cell rests again and the voltage converges to its open circuit voltage. The strain signal decreases with decreasing cell temperature and converges to its initial value.

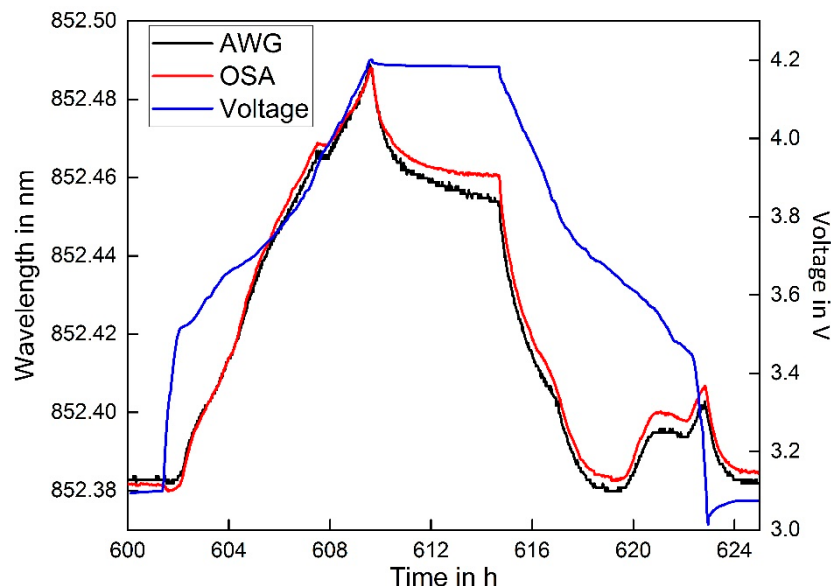


Figure 9. Exemplary single cycle showing the typical optically measured strain behavior of a lithium-ion cell along with the cell voltage.

4. Conclusions

With this work, we present a new, precise and cost-effective approach to read-out FBG utilizing a novel AWG interrogation system. The polymeric AWG are simple and cost-efficient to produce by using direct laser lithography, a technique that allows rapid development of integrated optical systems and enables short times from simulation to an operational prototype. For the application as a status monitoring device of lithium-ion batteries, the designed AWG interrogation system shows good optical performance. With a comparison to an optical spectrum analyzer, we calculated the approximate accuracy of our new measurement system to $\pm 7.59 \times 10^{-2}$ nm. The resolution is defined by the S-functions to 1×10^{-3} nm. The obtained accuracy is sufficient to observe the typical strain behavior (e.g., as in ref. [25,26]) of a single cell during one full charge cycle and was maintained for 25 cycles over one month. Nevertheless, the influence of the relative air humidity is not negligible and has to be investigated further. Although we are able to minimize the error with simple methods, the systems robustness has to be improved in order to become competitive to state-of-the-art electrical BMS. Besides this, future work will focus on AWG with at least 16 output channels to distinguish up to 8 FBG and to enable the usage of a reference FBG for temperature compensation in order to monitor a battery cell under non standardized conditions and extend the observations to a multitude of cells. The herein presented interrogation unit can furthermore be used to evaluate a multitude of FBG by using standard optical accessories e.g., an optical switch, or by using a multilayer design with several stacked AWG in combination with a two-dimensional CMOS image sensor to evaluate the individual output channel intensities. In future studies, the acquired optical information will be investigated in more detail for use in advanced algorithms that are able to exactly determine the SOC and SOH of a battery system. Furthermore, it is desirable to develop an all polymeric sensor system that consists not only of a polymeric AWG, but also takes advantage of other polymeric components, like a polymeric coupler and FBG.

Author Contributions: For the presented research work the authors are contributed in the following manner: J.M., A.N. and W.S. are responsible for the conceptualization and funding acquisition; J.M. and A.N. are responsible for data curation, investigation, methodology, visualization and writing; J.M. is responsible for formal analysis and software; A.N. and C.K. are responsible for project administration; E.P., C.K., A.N. and J.M. are responsible for resources; C.K. is responsible for validation; C.K., A.N. and J.M. are responsible for writing—review and editing; W.S is responsible for supervision.

Funding: This research was funded by the German Federal Ministry for Economic Affairs and Energy, grant number 03ET6105A.

Acknowledgments: Financial support for the conduction of the experiments from the Federal Ministry for Economic Affairs and Energy is gratefully acknowledged.

Conflicts of Interest: The authors declare no conflict of interest.

References

- Li, M.; Lu, J.; Chen, Z.; Amine, K. 30 Years of Lithium-Ion Batteries. *Adv. Mater. Weinheim*. **2018**, *30*, e1800561. [[CrossRef](#)] [[PubMed](#)]
- Zubi, G.; Dufo-López, R.; Carvalho, M.; Pasaoglu, G. The lithium-ion battery: State of the art and future perspectives. *Renew. Sustain. Energy Rev.* **2018**, *89*, 292–308. [[CrossRef](#)]
- Cano, Z.P.; Banham, D.; Ye, S.; Hintennach, A.; Lu, J.; Fowler, M.; Chen, Z. Batteries and fuel cells for emerging electric vehicle markets. *Nat. Energy* **2018**, *3*, 279–289. [[CrossRef](#)]
- Telaretti, E.; Dusonchet, L. Stationary battery systems in the main world markets: Part 1: Overview of the state-of-the-art. In Proceedings of the 2017 IEEE International Conference on Environment and Electrical Engineering and 2017 IEEE Industrial and Commercial Power Systems Europe (EEEIC/I&CPS Europe), Milan, Italy, 6–9 June 2017; pp. 1–7, ISBN 978-1-5386-3917-7.
- De Sisternes, F.J.; Jenkins, J.D.; Botterud, A. The value of energy storage in decarbonizing the electricity sector. *Appl. Energy* **2016**, *175*, 368–379. [[CrossRef](#)]
- Abada, S.; Marlair, G.; Lecocq, A.; Petit, M.; Sauvant-Moynot, V.; Huet, F. Safety focused modeling of lithium-ion batteries: A review. *J. Power Sources* **2016**, *306*, 178–192. [[CrossRef](#)]
- Feng, X.; Ouyang, M.; Liu, X.; Lu, L.; Xia, Y.; He, X. Thermal runaway mechanism of lithium ion battery for electric vehicles: A review. *Energy Storage Mater.* **2018**, *10*, 246–267. [[CrossRef](#)]
- Federal Aviation Administration. Aviation Cargo and Passenger Baggage Events Involving Smoke, Fire, Extreme Heat or Explosion Involving Lithium Batteries or Unknown Battery Types. 2018. Available online: https://www.faa.gov/hazmat/resources/lithium_batteries/media/Battery_incident_chart.pdf (accessed on 26 March 2019).
- Monhof, M.; Beverungen, D.; Klör, B.; Bräuer, S. Extending Battery Management Systems for Making Informed Decisions on Battery Reuse. In *New Horizons in Design Science: Broadening the Research Agenda*; Donnellan, B., Helfert, M., Kenneally, J., VanderMeer, D., Rothenberger, M., Winter, R., Eds.; Springer International Publishing: Cham, Switzerland, 2015; pp. 447–454. ISBN 978-3-319-18713-6.
- Rohr, S.; Wagner, S.; Baumann, M.; Muller, S.; Lienkamp, M. A techno-economic analysis of end of life value chains for lithium-ion batteries from electric vehicles. In Proceedings of the 2017 Twelfth International Conference on Ecological Vehicles and Renewable Energies (EVER), Monte-Carlo, Monaco, 11–13 April 2017; pp. 1–14, ISBN 978-1-5386-1692-5.
- Andrea, D. *Battery Management Systems for Large Lithium-Ion Battery Packs*; Artech House: Boston, MA, USA, 2010; ISBN 978-1-60807-104-3.
- Hannan, M.; Lipu, M.; Hussain, A.; Mohamed, A. A review of lithium-ion battery state of charge estimation and management system in electric vehicle applications: Challenges and recommendations. *Renew. Sustain. Energy Rev.* **2017**, *78*, 834–854. [[CrossRef](#)]
- Xiong, R.; Li, L.; Tian, J. Towards a smarter battery management system: A critical review on battery state of health monitoring methods. *J. Power Sources* **2018**, *405*, 18–29. [[CrossRef](#)]
- Cannarella, J.; Arnold, C.B. Stress evolution and capacity fade in constrained lithium-ion pouch cells. *J. Power Sources* **2014**, *245*, 745–751. [[CrossRef](#)]
- Lee, B. Review of the present status of optical fiber sensors. *Opt. Fiber Technol.* **2003**, *9*, 57–79. [[CrossRef](#)]
- Chen, J.; Liu, B.; Zhang, H. Review of fiber Bragg grating sensor technology. *Front. Optoelectron. China* **2011**, *4*, 204–212. [[CrossRef](#)]

17. Chikh-Bled, H.; Chah, K.; Álvaro, G.-V.; Caucheteur, C.; Lasri, B. Behavior of femtosecond laser-induced eccentric fiber Bragg gratings at very high temperatures. *Opt. Lett.* **2016**, *41*, 4048. [[CrossRef](#)]
18. Meyer, J.; Nedjalkov, A.; Doering, A.; Angelmahr, M.; Schade, W. Fiber optical sensors for enhanced battery safety. In Proceedings of the Fiber Optic Sensors and Applications XII. SPIE Sensing Technology + Applications, Baltimore, MD, USA, 20–24 April 2015. [[CrossRef](#)]
19. Nascimento, M.; Ferreira, M.S.; Pinto, J.L. Real time thermal monitoring of lithium batteries with fiber sensors and thermocouples: A comparative study. *Measurement* **2017**, *111*, 260–263. [[CrossRef](#)]
20. Yang, G.; Leitão, C.; Li, Y.; Pinto, J.; Jiang, X. Real-time temperature measurement with fiber Bragg sensors in lithium batteries for safety usage. *Measurement* **2013**, *46*, 3166–3172. [[CrossRef](#)]
21. Novais, S.; Nascimento, M.; Grande, L.; Domingues, M.F.; Antunes, P.; Alberto, N.; Leitão, C.; Oliveira, R.; Koch, S.; Kim, G.T.; et al. Internal and External Temperature Monitoring of a Li-Ion Battery with Fiber Bragg Grating Sensors. *Sensors* **2016**, *16*, E1394. [[CrossRef](#)]
22. Raghavan, A.; Kiesel, P.; Sommer, L.W.; Schwartz, J.; Lochbaum, A.; Hegyi, A.; Schuh, A.; Arakaki, K.; Saha, B.; Ganguli, A.; et al. Embedded fiber-optic sensing for accurate internal monitoring of cell state in advanced battery management systems part 1: Cell embedding method and performance. *J. Power Sources* **2017**, *341*, 466–473. [[CrossRef](#)]
23. Lochbaum, A.; Kiesel, P.; Sommer, L.W.; Bae, C.-J.; Staudt, T.; Saha, B.; Raghavan, A.; Lieberman, R.; Delgado, J.; Choi, B.; et al. Embedded Fiber Optic Chemical Sensing for Internal Cell Side-Reaction Monitoring in Advanced Battery Management Systems. *MRS Proc.* **2014**, *1681*, 715. [[CrossRef](#)]
24. Nedjalkov, A.; Meyer, J.; Gräfenstein, A.; Schramm, B.; Angelmahr, M.; Schwenzel, J.; Schade, W. Refractive Index Measurement of Lithium Ion Battery Electrolyte with Etched Surface Cladding Waveguide Bragg Gratings and Cell Electrode State Monitoring by Optical Strain Sensors. *Batteries* **2019**, *5*, 30. [[CrossRef](#)]
25. Bae, C.-J.; Manandhar, A.; Kiesel, P.; Raghavan, A. Monitoring the Strain Evolution of Lithium-Ion Battery Electrodes using an Optical Fiber Bragg Grating Sensor. *Energy Technol.* **2016**, *4*, 851–855. [[CrossRef](#)]
26. Sommer, L.W.; Kiesel, P.; Ganguli, A.; Lochbaum, A.; Saha, B.; Schwartz, J.; Bae, C.-J.; Alamgir, M.; Raghavan, A. Fast and slow ion diffusion processes in lithium ion pouch cells during cycling observed with fiber optic strain sensors. *J. Power Sources* **2015**, *296*, 46–52. [[CrossRef](#)]
27. Sommer, L.W.; Raghavan, A.; Kiesel, P.; Saha, B.; Schwartz, J.; Lochbaum, A.; Ganguli, A.; Bae, C.-J.; Alamgir, M. Monitoring of Intercalation Stages in Lithium-Ion Cells over Charge-Discharge Cycles with Fiber Optic Sensors. *J. Electrochem. Soc.* **2015**, *162*, A2664–A2669. [[CrossRef](#)]
28. Tosi, D. Review and Analysis of Peak Tracking Techniques for Fiber Bragg Grating Sensors. *Sensors* **2017**, *17*, 2368. [[CrossRef](#)]
29. Jackson, D.A.; Bennion, I.; Rao, Y.J.; Zhang, L. Dual-cavity interferometric wavelength-shift detection for in-fiber Bragg grating sensors. *Opt. Lett.* **1996**, *21*, 1556. [[CrossRef](#)]
30. Tsao, S.-L.; Peng, P.-C. An SOI Michelson interferometer sensor with waveguide Bragg reflective gratings for temperature monitoring. *Microw. Opt. Technol. Lett.* **2001**, *30*, 321–322. [[CrossRef](#)]
31. Kersey, A.D.; Berkoff, T.A.; Morey, W.W. Multiplexed fiber Bragg grating strain-sensor system with a fiber Fabry-Perot wavelength filter. *Opt. Lett.* **1993**, *18*, 1370. [[CrossRef](#)]
32. Jung, E.J.; Kim, C.-S.; Jeong, M.Y.; Kim, M.K.; Jeon, M.Y.; Jung, W.; Chen, Z. Characterization of FBG sensor interrogation based on a FDML wavelength swept laser. *Opt. Express* **2008**, *16*, 16552–16560.
33. Talahashi, H.; Oda, K.; Toba, H.; Inoue, Y.; Takahashi, H. Transmission characteristics of arrayed waveguide NxN wavelength multiplexer. *J. Light. Technol.* **1995**, *13*, 447–455. [[CrossRef](#)]
34. Sano, Y.; Yoshino, T. Fast optical wavelength interrogator employing arrayed waveguide grating for distributed fiber bragg grating sensors. *J. Light. Technol.* **2003**, *21*, 132–139. [[CrossRef](#)]
35. Tsuchizawa, T.; Yamada, K.; Watanabe, T.; Park, S.; Nishi, H.; Kou, R.; Shinohima, H.; Itabashi, S.-I. Monolithic Integration of Silicon-, Germanium-, and Silica-Based Optical Devices for Telecommunications Applications. *IEEE J. Select. Top. Quantum Electron.* **2011**, *17*, 516–525. [[CrossRef](#)]
36. Pichler, E.; Bethmann, K.; Kelb, C.; Schade, W. Rapid prototyping of all-polymer AWGs for FBG readout using direct laser lithography. *Opt. Lett.* **2018**, *43*, 5347–5350. [[CrossRef](#)]
37. Koch, J.; Angelmahr, M.; Schade, W. Arrayed waveguide grating interrogator for fiber Bragg grating sensors: Measurement and simulation. *Appl. Opt.* **2012**, *51*, 7718–7723. [[CrossRef](#)]
38. Gijsenbergh, P.; Wouters, K.; Vanstreels, K.; Puers, R. Determining the physical properties of EpoClad negative photoresist for use in MEMS applications. *J. Micromech. Microeng.* **2011**, *21*, 74001. [[CrossRef](#)]

39. Sethuraman, V.A.; Hardwick, L.J.; Srinivasan, V.; Kostecki, R. Surface structural disordering in graphite upon lithium intercalation/deintercalation. *J. Power Sources* **2010**, *195*, 3655–3660. [[CrossRef](#)]
40. Weng, C.; Sun, J.; Peng, H. A unified open-circuit-voltage model of lithium-ion batteries for state-of-charge estimation and state-of-health monitoring. *J. Power Sources* **2014**, *258*, 228–237. [[CrossRef](#)]



© 2019 by the authors. Licensee MDPI, Basel, Switzerland. This article is an open access article distributed under the terms and conditions of the Creative Commons Attribution (CC BY) license (<http://creativecommons.org/licenses/by/4.0/>).